Solid Immersion Lenses for Enhancing the Optical Resolution of Thermal and Electroluminescence Mapping of GaN-on-SiC Transistors

J.W. Pomeroy[1] and M. Kuball

Center for Device Thermography and Reliability (CDTR), H.H. Wills Physics Laboratory, University of Bristol, Bristol, BS8 1TL, U.K.

Solid immersion lenses are shown to greatly enhance optical spatial resolution when measuring AlGaN/GaN HEMTs, taking advantage of the high refractive index of the SiC substrates commonly used for these devices. Solid immersion lenses can be applied to techniques such as electroluminescence emission microscopy and Raman thermography, aiding the development device physics models. Focused ion beam milling is used to fabricate solid immersion lenses in SiC substrates with a numerical aperture of 1.3. A lateral spatial resolution of 300 nm is demonstrated at an emission wavelength of 700 nm and an axial spatial resolution of 1.7±0.3 μm at a laser wavelength of 532 nm is demonstrated; this is an improvement of 2.5× and 5×, respectively, when compared with a conventional 0.5 numerical aperture objective lens without a SIL. These results highlight the benefit of applying the solid immersion lenses technique to the optical characterization of GaN HEMTs. Further improvements may be gained through aberration compensation and increasing the SIL numerical aperture.

[1] Author to whom correspondence should be addressed. Electronic mail: James.Pomeroy@Bristol.ac.uk.

I. INTRODUCTION

The outstanding electrical properties of AlGaN/GaN High Electron Mobility Transistors (HEMTs), including high voltage and high current handling capacity, have been highly beneficial for state-of-the-art high-power/frequency microwave amplifiers.[1,2] GaN-based transistors are also increasingly being developed for high voltage switching applications, including power conversion with improved efficiency with respect to silicon-based technology. Although reliable AlGaN/GaN HEMT operation has been demonstrated in microwave amplifier applications, operating voltages and power densities are typically de-rated to ensure long term reliability. De-rating reduces the effect of channel temperature or electric field driven degradation mechanisms to a safe level. In order to achieve the full power handling potential of GaN based transistors, degradation mechanisms must be physically understood and then mitigated through device design. Reliability models require degradation drivers in operating devices, including temperature, electric field, hot electrons and strain, to be accurately quantified. Measuring these effects in GaN HEMTs is experimentally challenging because peak values occur in a sub-micron region close to the gate edge. For example, Joule heating and hot electrons are mainly confined to a high electric field region of the 2DEG, which is within <0.5μm of the gate edge.[3] Therefore, suitable measurement techniques should have a sufficiently high spatial resolution to ensure that that these effects are not underestimated due to spatial averaging. Microscopy based optical measurement techniques, including Raman thermography (measuring lattice temperature,[4] strain,[5,6] electric field[3]) and electroluminescence emission (measuring hot carriers[7] and leakage pathways[8,9]), have been used extensively to analyze AlGaN GaN HEMTs. Raman thermography, based on measuring the temperature induced phonon frequency shift induced in scattered laser light enables lateral and depth temperature profiles to be measured with a high lateral (0.5-0.6 μm) and temporal resolution (~10ns).[3,4,10] The same technique has also been used to investigate piezoelectric induced strain in voltage biased devices, via the phonon frequency shift induced by mechanical strain.[5] An advantage of micro-Raman scattering, with regard to surface sensitive techniques such as reflectance, is that 3D confocal mapping of material properties can be performed through transparent materials; e.g., the GaN epitaxial layer and SiC substrate of an AlGaN/GaN HEMT. Three dimensional temperature mapping has enabled the effect of thermal boundary resistance on heat flow across the interface between heteroepitaxial layers and substrates to be quantified in GaN HEMTs.[11,12] Hot electron electroluminescence also generated by the presence of the high electric field region can also be studied optically: both location of high electric and electron temperature can be obtained by measuring the emitted light,[7] and the breakdown location in devices subjected to electrical stress.[8,9]

Although these techniques do offer comparatively high spatial resolution, in particular when compared to electrical measurement techniques which measure a spatial average over the whole device periphery, even more information could be

gained by further enhancing spatial resolution. For example, true 3D nanometer optical resolution would enable the predicted effect of non-continuum thermal transport on channel temperature in AlGaN/GaN HEMTs to be investigated experimentally,[13] or locate areas of degradation more precisely after electrical stress. Optical resolution is fundamentally limited by the numerical aperture (NA) of the light focusing and collection optics, which has a maximum value equal to the refractive index (n) of the immersion (focusing) medium. This immersion medium is typically air, having n=1: Although the theoretical NA limit for an air immersion lens is 1, the experimentally achievable NA limit is determined by the minimum working distance required to accommodate probe tips or device packaging. Previously reported micro-Raman thermography or electroluminescence microscopy measurements have been performed using an objective lens with an NA~0.5, enabling sufficient working distances of >5mm.[3-6,8-11,14-17] The optical resolution provided by an 0.5 NA objective lens is therefore used as a benchmark in this paper. We also note that when focusing onto the backside of a device through a transparent substrate, which is advantageous when the active part of the device is obscured by metal on the top side, for example, under the gate and field plates,[9,15] optical resolution is aberration limited. In this case, refraction induces spherical aberration which mainly degrades the depth of focus,[18] particularly for high refractive index substrates such as SiC (n=2.65).

The solid immersion lens (SIL) technique can be used to increase NA in high refractive index materials, such as the SiC substrate, without aberration due to mismatched refractive indices,[19] which is potentially very beneficial for back-side (through substrate) optical measurements of GaN HEMTs. A SIL is effectively a lens integrated into the material being measured. Aberration free foci can then be formed at two aplanatic points within a sphere: At the center of the sphere, so that the lens forms a hemispherical SIL (h-SIL), e.g., as illustrated in Fig. 1(a), and at a focal point offset from the center of the sphere, determined by the SIL refractive index, to form a truncated spherical lens called a super-SIL (not shown).[20] Of the two approaches, the h-SIL is the most appropriate for device measurements, having the following advantages over the s-SIL: A greater lens thickness tolerance, greater field of view and negligible chromatic or birefringence induced aberration.[21] The h-SIL increases the NA and magnification by a factor of n, with respect to a standard air immersion objective.[20] The h-SIL also reduces lateral or axial translation of the focal point by a factor of n, due the optical lever effect.[22]

SILs have been implemented in two ways for back-side device measurements: Focusing through a separate lens placed on the sample surface,[19,22] or forming the substrate into solid immersion lens, as illustrated in Fig. 1(a), e.g., milled using diamond turning.[23] The former method has the advantage that the lens can be moved across the back side of the device to the regions of interest, although a large enough opening is required to accommodate the SIL which may not be practical in all cases.[24] Another consideration when using a plano-convex SIL is that the air gap should be kept below 0.2λ to avoid internal reflection at the interface between the SIL and device backside which can limit the achievable NA .[21] SILs formed by diamond turning in silicon

substrates have been demonstrated with diffraction limited performance;[23] This approach has the advantages of a reduced lens size, potentially requiring a smaller opening in the device package, and since the lens is integrated into the device substrate, no air gap. A versatile alternative SIL fabrication technique based on focused ion beam (FIB) micro-machining has been developed to form solid immersion lenses in silicon;[25-27] this approach can also be applied to hard materials, including SiC.[24] The challenge of the FIB approach is overcoming the non-linearity associated with focused ion beam milling to achieving a high lens shape accuracy.[24,27]

SiC substrates are an ideal candidate for SIL fabrication due to their high refractive index and therefore potentially high NA. In this work, h-SILs are formed in SiC substrates for enhanced optical resolution back-side measurements of AlGaN/HEMTs. Due to the difficulty of mechanically machining high hardness SiC, we have adapted the focused ion beam micro-machining method of Ref. 25, developing and in-situ lens shape correction method to achieve a high lens shape accuracy. The optical resolution enhancement provided by the SIL is applied to electroluminescence microscopy and Raman thermography measurements of AlGaN/GaN HEMTs.

II. SIL DESIGN

The optical resolution of a focusing lens is related to the numerical aperture (NA)

$$NA = n \cdot sin\theta \quad , \tag{1}$$

where n is the refractive index of the immersion (focusing) medium and θ is the half angle of the focused cone of light (illustrated in Fig. 1(a)). The maximum NA is equal to the refractive index n, e.g., in the case of air is $NA_{MAX\ air} = n_{air} = 1$, whereas for SiC $NA_{MAX\ SiC} = n_{SiC} = 2.6$. The diffraction limited lateral and axial resolution are given by

$$r_{lateral} = \frac{0.51 \cdot \lambda}{NA} \quad , \tag{2}$$

and

$$r_{axial} = \frac{0.88 \cdot \lambda}{\left(n - \sqrt{n^2 - NA^2}\right)} \ , \tag{3}$$

respectively, where λ is the wavelength of the focused/collected light.[28] The pre-factors in Eq. (1) and (2) are reduced to 0.37 and 0.51, for the lateral and axial resolution respectively, when using confocal detection (detection pin-hole diameter << point spread function FWHM). Figure 1(c) illustrates the improvement in lateral and axial spatial resolution from NA=0.5 up to NA=2.65, with NA=0.5 being a typical value when using standard microscopy for device measurements and 2.65 being the

upper limit for a SiC SIL. The lateral resolution is inversely proportional to the NA, whereas the axial resolution is approximately inversely proportional to the square of NA.

Optical aberration should be considered when there is a refractive index mismatch between the substrate and heteroepitixial device layers. For example, SIL numerical aperture may be restricted for silicon-on-insulator (SOI) technology with thick insulator layers, owing to the refractive index contrast between the insulator layer and the high refractive index silicon wafer. For GaN-on-SiC the refractive index of the GaN layer and SiC substrate are similar, e.g. n_{GaN} = 2.43 versus n_{SiC}=2.65 at a wavelength of 532 nm, and the GaN/SiC interface can be considered aberration free for typical GaN layer thicknesses. Therefore we include the GaN layer in the total thickness of the SiC substrate when analyzing the GaN-on-SiC SIL design. When focusing close to the surface of GaN or SiC from air, the diffraction limited confocal lateral and axial resolution for an 0.5 NA objective lens is 0.55 µm and 10 µm, as given by Eq. (2) and Eq. (3), respectively. We note that the axial resolution is much larger than the typical 1-2µm thickness of the epitaxial GaN layer in a microwave AlGaN/GaN HEMT, making it impossible to resolve different depths within this layer. Raman thermography therefore measures the temperature averaged through the depth of the GaN layer.[4] In comparison, the theoretical limit for the lateral and axial resolution of a SiC SIL is 130 nm and 100 nm, respectively. Although it is practically difficult to achieve the maximum NA (θ=90°), improving NA beyond the NA=1 air immersion limit can enable high-resolution 3-D scanning microscopy within the GaN layer, in particular around the active region close to the transistor gate. In this work, we combine a standard 0.5 NA microscope objective (θ=30°) with a SiC SIL to achieve an NA of 1.3, having a potential diffraction limited resolution of $r_{lateral}$ = 0.15µm and r_{axial} = 1 µm at a wavelength of 532 nm.

Another consideration for imaging and scanning applications are the allowances for aberration (W) which can be tolerated without degrading the SIL focusing performance. Two possible causes of aberration are changing the lens thickness (a) from its ideal value and focusing off center laterally (b), which relates to the useable field of view. The lens thickness tolerance is relevant for axial scanning measurements such as depth mapping using Raman thermography. Baba has derived allowances for thickness error $|a|$ and field of view diameter $2b$ satisfying the, $W<\lambda/4$ "quarter wavelength condition" for h-SILs, which in the limit of sin θ = 1 are given by :[21]

$$|a| < \left[\frac{2R\lambda}{n(n-1)}\right]^{1/2}, \tag{4}$$

and

$$2b < \left[\frac{2R\lambda}{n(n-1)}\right]^{1/2}, \tag{5}$$

where *R* is the spherical radius of the lens, corresponding to the ideal lens thickness for a hemispherical SIL. Using Eq. (4) and Eq. (5), the lens thickness tolerance and usable field of view for a SiC hemispherical SIL with a radius of 40μm can be calculated as ±3.1μm and 6.2 μm respectively. These allowances are lower limits values and are relaxed when sin θ<1. The ±3.1 μm lens thickness tolerance is large enough to accommodate translation of the focus through the GaN layer. To verify the useable field of view ray tracing was performed[29] to calculate the wavefront error caused by translating a point emission source laterally from the optimal focal point aligned with the lens optical axis, as illustrated in the inset of Fig. 2. The Strehl (*S*) ratio was used to evaluate the effect of wavefront aberrations on image quality, using the Mahajan expression:[30]

$$S \cong e^{-\sigma_\phi{}^2}\,, \tag{6}$$

where $\sigma_\phi{}^2$ is the wavefront phase variance in wave units. A Strehl ratio >0.8 corresponds to image quality that is effectively diffraction limited. Based on the results shown in Figure 2, good imaging performance is expected over a ~14 μm field of view for a 1.3 NA SiC h-SIL with a radius of 40 μm. The aspheric error allowance, *c*, should also be considered when fabricating the h-SIL. By satisfying the quarter wavelength aberration condition, the maximum allowable deviation of the lens surface from a perfect hemisphere is given by:[21]

$$c < \frac{\lambda}{4(n-1)}\,. \tag{7}$$

For example, to achieve close to the optimal performance from a SiC h-SIL at a wavelength around 500 nm, the aspheric error should be below ~100 nm.

II. SIL Fabrication and Testing

AlGaN/GaN HEMT on SiC wafers were used for this study, consisting of a typical epilayer stack: AlN nucleation layer, a 1.2 or 1.9 μm-thick GaN epilayer, and a 10s of nm thick AlGaN barrier layer. A 2DEG conduction channel is formed close to the surface at the interface between the GaN buffer and the thin AlGaN barrier. In order to minimize FIB milling time, the SiC substrate was mechanically back-thinned from 330 μm to 40 μm, prior to SIL fabrication. Following thinning, the surface was chemical-mechanically polished in order to ensure that substrate surface was smooth before proceeding with the FIB milling process. Focused gallium ion beam milling was performed using a dual beam FEI HELIOS Nanolab 600 FIB system, using a 21 nA beam current and 30 KeV accelerating voltage. The ideal hemispherical lens surface was calculated, having a spherical radius *R* equal to the total thickness of the substrate and epilayer, as illustrated in Fig. 1(a). The lens is oversized (θ>30°) to ensure that the focused light cone can be completely accommodated. For comparison, previous SILs fabricated by FIB in silicon

substrates have a maximum half angle of θ=22°.[26] Figure 3(b) shows a profile of the hemispherical lens design: In summary, the design has a total diameter is ~120μm and the maximum milled depth is ~20 μm.

A reticle, visible in the SEM image of Fig. 3(a), was at first placed to align the center of the SIL with the area of interest, which in this case is directly underneath the transistor gate. A stream file was used to control the FIB dwell time at each coordinate in the milling pattern. Short dwell times (<10 μsec) were used to minimize redeposition during milling.[31] The dwell time at each point (t_{dwell}) was set to be proportional to the required milled depth at each point on the designed lens surface, after calibrating the material removal rate (0.6 $\mu m^3 nA^{-1}s^{-1}$); the total milling depth at each point was then controlled by adjusting the total number of repetitions of the milling pattern. Gas assisted etching (GAE) was not used due to the non-linear relationship between dwell time and milling rate.[32] Milling was performed by following an Archimedean spiral, starting at the lens center and working outwards, again to minimize material deposition.[31] The spacing between each dwell point was set to 0.3 μm, ensuring a >50% beam overlap at the 21 nA beam current used to ensure a smooth surface after milling.

To compensate for non-linearity during the milling, primarily caused by re-deposition and the varying beam angle of incidence,[31] a multistep iterative procedure was developed in which the lens shape was milled, the surface profile measured in-situ and a subsequent corrective milling pass used to correct the lens surface profile; performing the lens shape optimization in-situ has the advantage of being non-destructive and rapid, with respect to cross sectioning or ex-situ AFM measurements,[25] respectively. The first milling iteration was performed by adjusting dwell times to match the required depth, then reducing the dwell times by a damping factor of 0.8 to ensure that over-milling did not occur at any point on the lens surface. The shape of the lens surface shape is then measured in-situ by depositing a 100 nm-wide platinum strap across the lens diameter, visible in Figure 3(a). The lens is then tilted along the axis of the platinum strap to an angle of 45° to enable the lens surface profile to be imaged by scanning electron microscopy (SEM), as illustrated in Fig. 3(a). The lens surface profile is then obtained by performing image processing to trace the visible line at the interface between the platinum strap and SiC surface, correcting the resulting dimensions for the tilted viewing angle. Figure 3(b) shows a comparison of the lens surface profile with the designed lens shape after the first iteration; we observe the largest deviation towards the outer part of the lens, where most redeposition occurs. A second corrective milling iteration is then performed by setting the milling depth to be equal to the difference between the milled and designed lens shape across the lens surface, i.e., the lens shape error. The correction was applied in polar coordinates as a function of radial distance from the center of the lens, assuming rotational symmetry. Figure 3(a) shows an SEM image of a completed lens. In total ~100,000 μm^3 of material is removed in ~4 hours. The lens shape accuracy was evaluated after the second milling step by depositing a second platinum strap on the lens surface, following the process described previously. A high lens shape accuracy is achieved across most of the lens surface along the measured axis,

as shown in Fig. 3(b). We note that although the platinum strap remains on the lens surface after processing, it does not degrade the lens performance since it is thin with respect to visible wavelengths and far from the SIL focal plane. The lens aspheric aberration shown in Fig. 3(c) is close to or within the $1/4\lambda$ condition given by Eq. (6) over most of the lens surface, although deviations are observed close to the outer part of the lens. Finally, a cleaning step was performed by using a XeF_2 gas assisted etch at a low beam current to remove 100 nm of SiC, including an amorphous Ga implanted layer; this was required to restored optical transparency, as noted in Ref [25].

Atomic force microscopy (AFM) was performed following the fabrication to further evaluate the symmetry and surface roughness of the SIL. Figure 4(a) shows a comparison between the designed lens shape and the AFM measured profile measured across the SIL diameter in orthogonal directions, denoted X and Y, as illustrated in the inset schematic. The AFM measured profile closely matches the designed profile along axis X, which is aligned with the platinum strap used for the in-situ shape correction. However, the measured lens surface profile deviates from the design along the Y direction, with a maximum deviation of ~500 nm. Although the error in the lens shape in the Y direction is not large, it is greater than the 100 nm aspherical limit given by Eq. (7), and hence the astigmatism introduced will potentially reduce the optical performance of the lens. Fig. 4(b) illustrates the roughness of the milled lens surface, flattened by subtracting the designed profile. A surface wave with a 30nm RMS deviation and 6 μm period is observed and attributed to the ion milling process. Therefore the deviation of the resulting lens from the designed lens shape, rather than surface roughness is the main limitation for optical performance. Because milling was performed in a spiral pattern outward from the center of the lens, we attributed the asymmetry observed in Fig. 3(b) and Fig. 4(a) to either drift of the ion beam position relative to the sample surface or imperfect realignment of the beam pattern during the second milling iteration.

The resulting SiC SIL was evaluated by performing confocal micro-Raman thermography and electroluminescence emission measurements. We compare a standard 50× magnification 0.5 N.A objective lens used in the most optimal configuration, that is focusing from the device top-side, to the same lens combined with the 1.3 NA SiC SIL, focusing through the substrate. To enable the backside measurements, a 2 mm diameter aperture was made in the copper heatsink beneath the device under test. The measured transistors have two 100 μm-wide gates and a gate-gate pitch of 50 μm. Raman scattering measurements were performed using a confocal Renishaw inVia micro-Raman spectrometer with 532 nm laser excitation and unpolarised back-scattering detection. Mapping measurements were performed by translating the SIL with respect to the objective lens, using a motorized XYZ translation stage with a step precision of 0.1 μm and correcting for the $\times n$ reduction in translation when focusing through h-SIL, due to the optical lever effect.[22] Electroluminescence images were collected using a thermoelectrically cooled CCD. More details of the analysis of GaN HEMTs using Raman thermography and

electroluminescence microscopy can be found in Refs. [3,4,6,11,15] and Refs. [7,9,17], respectively. All measurements were performed at an ambient temperature of 22°C.

Three dimensional finite element thermal modelling was performed for comparison to the measured device temperatures. The model includes the GaN-on-SiC wafer and heatsink with an opening below the active device. Room temperature thermal conductivity values of 160 W/mK (with a $T^{-1.4}$ temperature dependence) and 420 W/mK (with a $T^{-1.2}$ temperature dependence) were used for the GaN and SiC layers, as in Ref. [33].An effective interfacial thermal resistance was included between the GaN and SiC in the model with a room temperature value of 1.5×10^{-8} m^2K/W and a temperature dependence of $T^{1.1}$, based on Ref. [16]. An 0.5 µm-long heater was placed adjacent to the drain edge of the gate, at the AlGaN/GaN interface representing the high electric field Joule heating region.[3]

IV. Results and Discussion

A. Electroluminescence Microscopy

A transistor was subjected to a high negative gate voltage off state stress similar to Ref. [17], generating localized electroluminescence emission "hot spots". These EL emission points are associated with the formation of highly localized current leakage pathways, electrically shorting the gate to the 2DEG through the AlGaN barrier.[8,17] These emission regions are expected to be much smaller than the EL emission wavelength and are confined to the 2DEG at the AlGaN/GaN interface. Off state EL emission is therefore optimal for evaluating the lateral resolution of the SIL. Figure 5(a) shows an image of EL emission image collected from the top side of the device using the 0.5 NA objective lens. EL emission is observed at the drain edge of the gate in the standard microscope image, where the electric field is located.[8,9,17] However, identification of the exact location of the emission is lacking due to the finite spatial resolution, which is ~750 nm around the peak detected EL emission wavelength of 700-800 nm. Figure 5(b) shows the SIL-enhanced EL image, individual EL emission spots are clearly resolved and can be unambiguously located, exactly at the gate edge where the peak electric field is predicted. A weak emission spot at the source edge of the gate, magnified as an inset of Fig. 5(b), is also resolvable in the SIL EL image and is attributed to a secondary electric field peak at this location, which is not resolvable in the standard microscope image. The measured FWHM of the smallest emission spot at the center of the image is ~300nm, which is close to the aberration free lateral SIL resolution of 270 nm, given by Eq. (2) at the peak detected EL emission wavelength. The ~2.5× improvement in lateral optical resolution when using SIL-enhanced EL microscopy clearly demonstrates the advantage of using SILs in this application, revealing details not observed in the standard EL image. The usable field of view when imaging using the SIL is estimated to be around 15 µm

based on the image shown in Fig. 5(b), which is large enough to span the typical source-drain opening in AlGaN/GaN HEMTs. The experimentally evaluated field of view closely matches the estimated ~14 μm field of view based on the ray tracing results shown in Fig. 2.

B. **Micro-Raman Thermography**

Figure 6(a) overlays Raman spectra measured when focusing into the GaN layer using the h-SIL through the SiC substrate (1.3 NA) and without h-SIL from the top side (0.5 NA). We observe a relative 5.5× increase in the GaN Raman scattering intensity with respect to phonon lines originating from the SiC substrate when using the SIL, indicating a shallower depth of focus; this compares favorably with the predicted 7× improvement in depth of focus predicted in Fig. 1(c). The 657 cm^{-1} AlN E_2 phonon line, attributed to the 40 nm thick nucleation layer between the SiC substrate and GaN epilayer, is observed in the spectra measured using the SIL but not in the spectra measured without SIL, even for extended integration times. The AlGaN E_2 phonon line originating from the thin barrier layer was not observed owing its lower cross section and proximity to the GaN E_2 peak.[34] Additionally, although they strictly are forbidden in the Z(X-)$\underline{Z}$ backscattering geometry, the GaN A_1(TO) and E_1(TO) phonon lines are observed weakly in the Raman spectrum recorded using the SIL, although not in the Raman spectrum recorded using the 0.5 NA lens. The observation of these modes is due to the increased maximum angle of incidence enabled by the SIL, in this case up to 30°, which introduces a significant out-of-plane polarization component. In comparison, the maximum half angle is reduced by refraction when focusing below the surface without the SIL, as illustrated in Fig. 1(b), e.g., $\theta<12°$ for the NA=0.5 case.

In order to estimate the SIL depth of focus, a depth scan was performed though the AlGaN/GaN HEMT layer structure, illustrated in Fig. 6(b) which shows the normalized Raman intensity of AlN and GaN E_2 modes recorded as a function of depth. The centers of the AlN and GaN layers are resolved as peaks in the Raman intensity profile separated by 0.6 μm, half the GaN layer thickness. The confocal depth resolution estimated from the AlN depth intensity profile is 1.7±0.3μm FWHM; this is valid since the thickness of the AlN layer is negligible with respect to the depth of focus. The measured depth of focus value is larger than the prediction of 1 μm for the 1.3 NA SIL, although it is a ~5× improvement over the confocal depth resolution measured for the 0.5 NA objective lens without the SIL, which is 10 μm. The 5× improvement in confocal depth is consistent with the relative 5.5× increase in the GaN Raman intensity observed in Fig. 6(a). The lower than predicted SIL depth of focus obtained is attributed to aberration caused by lens aspheric error, e.g., as illustrated in Fig. 3(c) and Fig. 4(a).

Figure 7(a) shows the simulated GaN HEMT depth temperature profile through a 1.9 μm-thick GaN layer; We note that ~50% of the total temperature rise across the GaN layer occurs within the first 0.5 μm below the AlGaN/GaN interface, owing to the relatively high GaN thermal conductivity of 160 W/mK, e.g., with respect to the 50 W/mK thermal conductivity of a

GaAs HEMT, combined with the highly localized power dissipation in the channel. The optimal depth resolution calculated for the designed 1.3 NA lens is overlaid. To evaluate the axial and lateral temperature gradient in the GaN layer during HEMT operation, lateral GaN temperature profiles were measured in the vicinity of the gate using the SIL, focusing at two depths within the GaN layer at a power dissipation of 2.26 W (11.3W/mm): The upper region at the AlGaN/GaN interface, and the lower region at the GaN/AlN interface, illustrated schematically in the inset of Fig. 7(a). We observe that the peak temperature is located at the drain edge of the gate in the measured temperature profiles, shown in Fig. 7(b), where most of the Joule heating is generated.[3] A temperature difference of ~10°C is measured between the upper and lower GaN temperature profiles, attributed to the temperature gradient through the GaN layer depth. The temperature gradient measured through the GaN layer depth is less than the 100°C simulated temperature difference across the GaN layer, shown in Fig. 7(a), due to depth spatial averaging: The depth of focus evaluated for the SIL is 1.7±0.3 μm, which is similar to the 1.9 μm GaN thickness layer of the measured HEMT and therefore both measured temperature profiles are similar to the simulated depth averaged GaN temperature. For comparison, the depth average GaN temperature, which corresponds to the conventional Raman thermography measurement, is also shown in Fig. 7(b) and lies between the measured upper and lower GaN temperature profiles. Although the vertical temperature gradient measured through the GaN layer is less than the predicted temperature gradient owing to spatial averaging, the experimental observation of a temperature gradient within the GaN layer does illustrate the feasibility of using the SIL technique for 3D temperature mapping within the GaN epilayer close to the transistor gate.

Thinning of the SiC substrate and forming an opening in the heat sink to gain optical access for the SIL measurement introduced an additional 60°C increase in the peak channel temperature; this was evaluated by comparing the thermal modelling result for the experimental SIL configuration against an un-thinned substrate and heatsink without an opening. Channel temperature remained within a safe operating range despite the additional temperature rise and IV characteristics (saturated drain current and pinch-off voltage) monitored before and after measurements showed no evidence of electrical degradation. However, since the SIL Raman thermography measurement is aimed at mapping the temperature within the GaN layer, the additional temperature rise due to imperfect heatsinking may be treated as an offset. This temperature offset can be minimized by reducing the amount of substrate thinning, although this would correspondingly increase the fabrication time.

To further improve the SIL depth of focus and enable 3D temperature mapping within the GaN layer, close to the 2DEG channel, the SIL optical resolution attained can be improved in two ways: Firstly aberration reduction and then increasing the NA. The aberration free depth of focus predicted for the 1.3 NA SIL is 1 μm, which is ~1/2 of the GaN layer thickness for the HEMT illustrated in Fig. 7(a). In comparison, the experimental depth of focus evaluated for the fabricated 1.3 NA SIL is 1.7±0.3 μm. We attribute this reduced optical resolution in aberration caused by deviations from the ideal lens surface profile,

for example, as illustrated in Fig. 1(c). To compensate for such aberration, wave front correction may be been applied using a deformable mirror, achieving an optical resolution closer to the diffraction limited value.[35] Increasing the SIL numerical aperture, in combination with aberration compensation, will further increase the potential depth of focus. A 2.0 NA SIL, could for example achieve a depth of focus of 0.5 μm, which is 1/4-1/3 of the typical GaN layer thickness in a microwave AlGaN/GaN HEMT, illustrated as an inset in Fig. 7(a).

V. CONCLUSION

By fabricating solid immersion lenses (SILs) to take advantage of the high refractive index of SiC substrates commonly used for microwave AlGaN/GaN HEMTs, the spatial resolution of optical measurements is significantly improved and can be applied to techniques including electroluminescence emission imaging and Raman thermography. Such improvements provide more detailed data for thermal and reliability models to further the understanding of device degradation mechanisms. A multistep focused ion beam milling process has been implemented to fabricate a 1.3 NA SiC solid immersion lens with high lens shape accuracy. The optical performance of the lens has been assessed by performing electroluminescence emission microscopy and Raman thermography measurements, and compared to the same measurements performed using a standard microscope objective lens. A 2.5× and 5× improvement in lateral and axial spatial resolution has been measured for a 1.3 NA h-SIL with respect to measurements performed using a standard 0.5 NA microscope objective lens. Electroluminescence hot spots, associated with localized electrical breakdown in degraded devices, have been unambiguously identified at the gate edge using the fabricated solid immersion lens, including details unresolvable with the standard objective lens alone. Lateral and vertical temperature gradients have been measured directly in the GaN buffer using the SIL; the later result demonstrates an axial spatial resolution less than the GaN layer thickness. In order to measure the peak channel temperature directly and map the GaN temperature close to the gate in 3-D, which is relevant for assessing thermally accelerated degradation mechanisms, axial spatially resolution must be further improved to $<<1\mu m$, which may be achieved by reducing lens aspheric error and increasing the SIL NA.

ACKNOWLEDGEMENTS

We are grateful to Dr. Peter Heard of the Interface Analysis Centre, University of Bristol, for technical advice regarding the focused ion beam instrument operation and Dr. Huarui Sun of the School of Physics, University of Bristol, for performing AFM measurements. This work supported in part by the by the EDA Manufacturable Gallium Nitride (MANGA) project and EPSRC grant number EP/L007010/1.

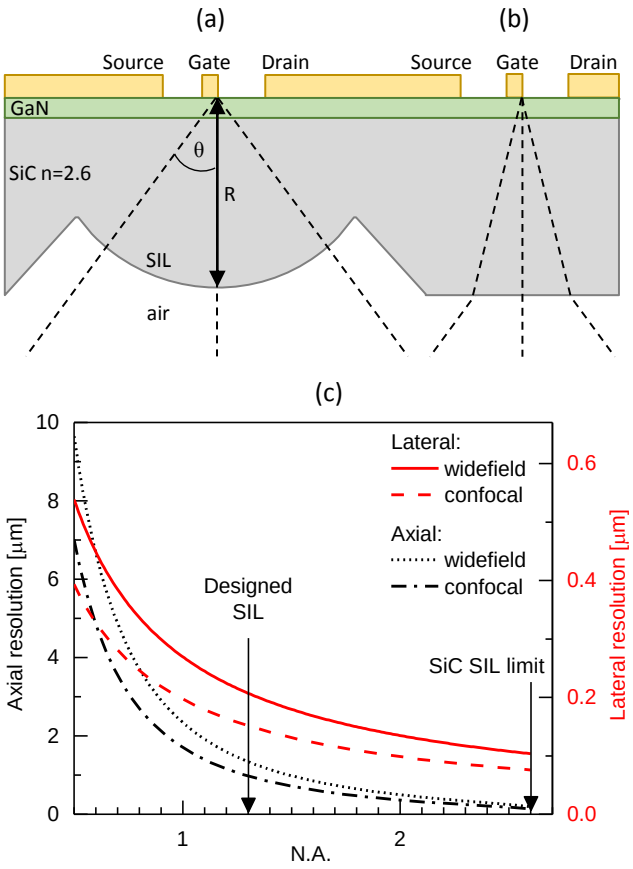

Figure 1: (a) Schematic illustration of a hemispherical solid immersion lens formed in the SiC substrate beneath an AlGaN/GaN HEMT, enhancing spatial resolution with respect to the standard focusing condition shown in (b). The solid immersion lens half angle θ, related to the numerical aperture, and lens radius R, are indicated. (c) The ideal, diffraction limited axial and lateral spatial resolution as a function of numerical aperture NA, for a confocal and non-confocal microscope at a wavelength of 532 nm. The resolution of the designed 1.3 N.A. SIL is highlighted and compared with the theoretical limit for a SiC SIL (N.A. = 2.65).

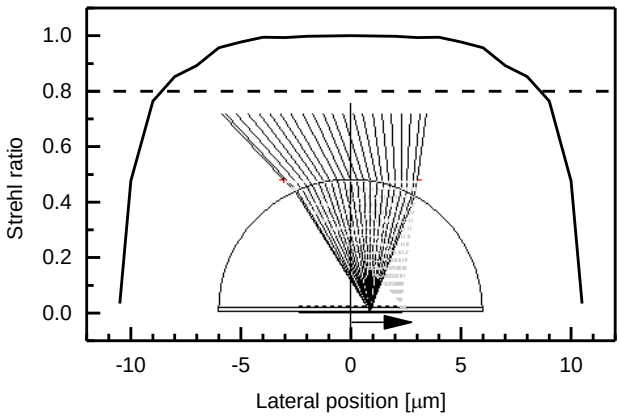

Figure 2: Ray tracing is performed to estimate the wavefront error as a function of the lateral distance from the optical axis of a 40 μm radius hemispherical SIL, illustrated as an inset. The Strehl ratio is used to evaluate imaging performance; values above 0.8 indicate that the imaging performance is effectively diffraction limited, indicated by the horizontal dashed line.

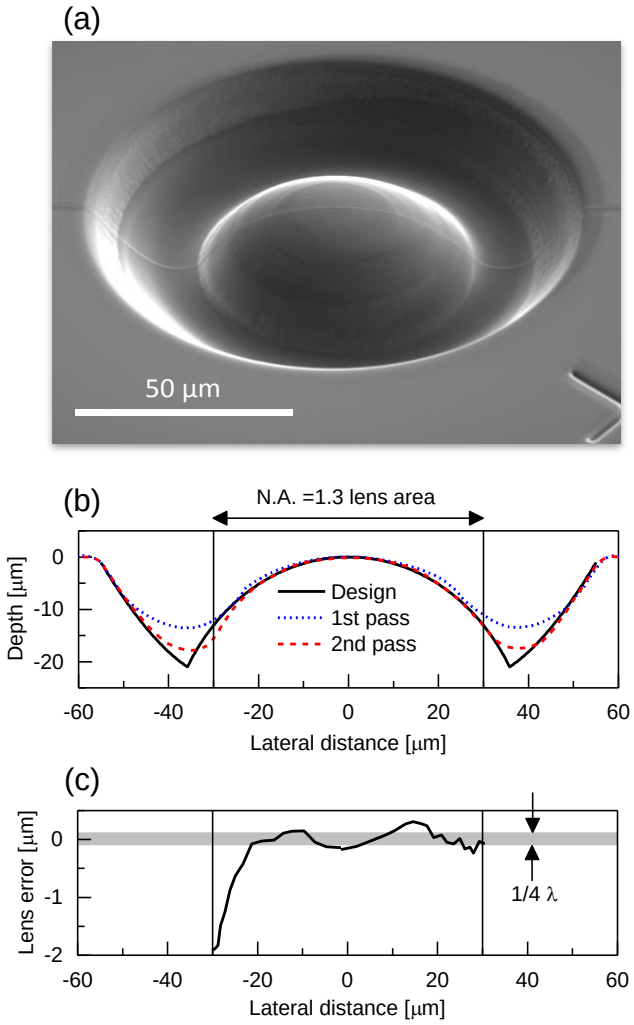

Figure 3: (a) SEM image of a fabricated SiC solid immersion lens titled at a 45° angle. The 100 nm-wide Pt strap on the lens surface is visible and was used for in-situ shape measurement. The reticle in the lower right hand corner was used as an aid for lens alignment with respect to area of interest around the transistor gate, located on the opposite site of the wafer. (b) In-situ measured lens surface profiles after the first and second milling iterations, compared to the designed lens shape, plotted in the actual aspect ratio. (c) The final residual error in the lens shape in the radial (light propagation direction). For visual reference the 1/4 λ lens surface variation required to minimize aspheric aberration is shaded.

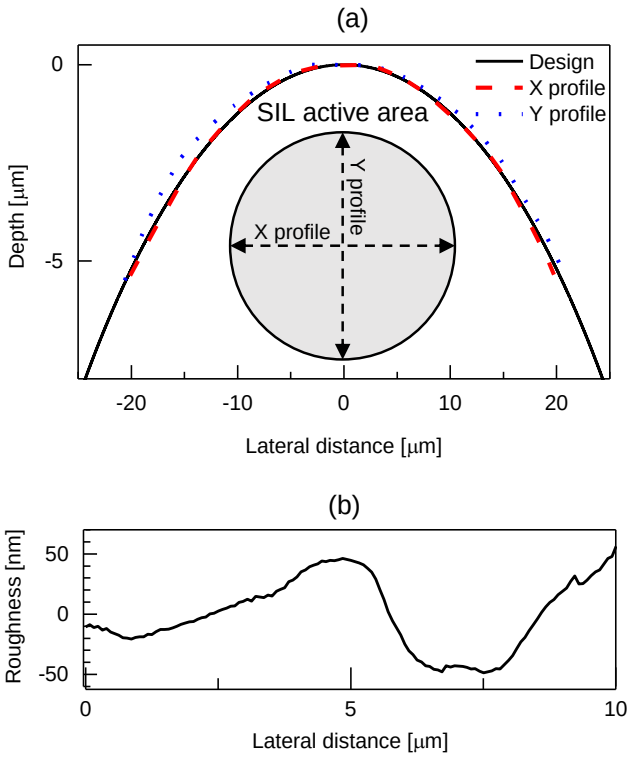

Figure 4: SIL surface measured by atomic force microscopy, showing: (a) Measured lens profile in the central portion of the lens, along two axis as illustrated in the inset plan-view schematic, compared with the designed profile; (b) A magnified view of the measured lens surface, flattened by subtracting the designed lens shape to evaluate surface roughness.

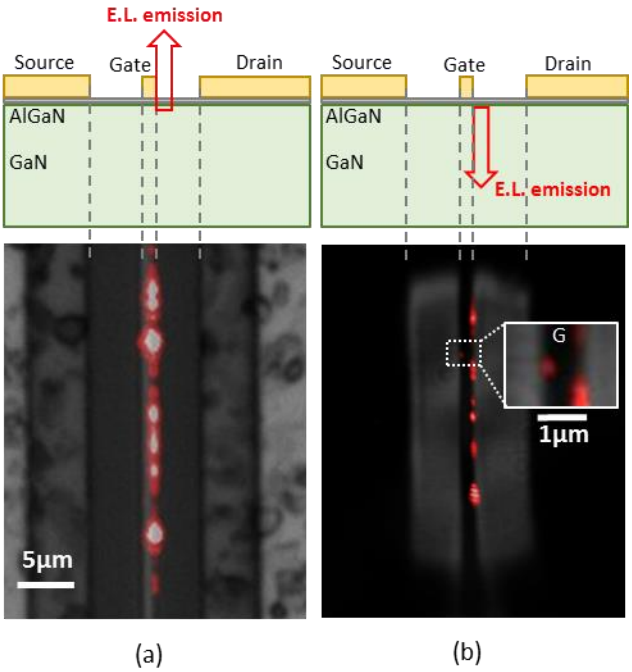

Figure 5: Comparison of electroluminescence (EL) emission images of a degraded AlGaN/GaN HEMT in pinch off at $10V_{sd,}$ $-5V_{gs}$ and 2.2 mA $I_{gate:}$ (a) Measured from the top side using a standard 0.5 N.A. objective lens and (b) through the SiC substrate via the SIL. The image shown in (a) has been scaled by 2.6× match the field of view shown in the SIL enhanced image (b). The images shown in (a) and (b) are a composite of the measured EL emission (red) and white light illumination image (greyscale). The white light illumination images in (a) and (b) were recorded in reflection and transmission, respectively. The schematic cross sections above the EL images show the location of contacts and the EL emission direction collected in (a) and (b). An enlarged portion of the gate in the SIL enhanced EL image is shown in (b), highlighting weak EL emission at the source edge of the gate.

(a)

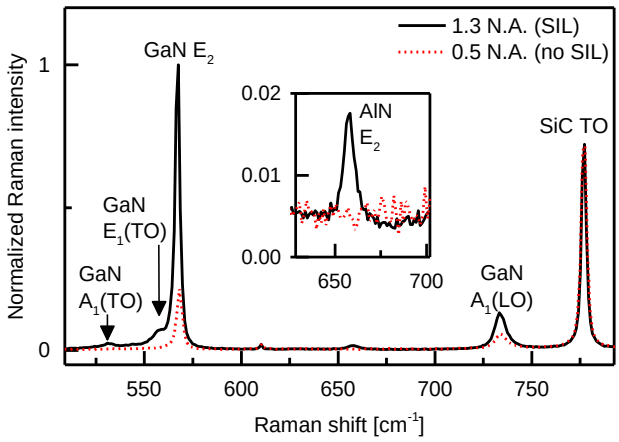

(b)

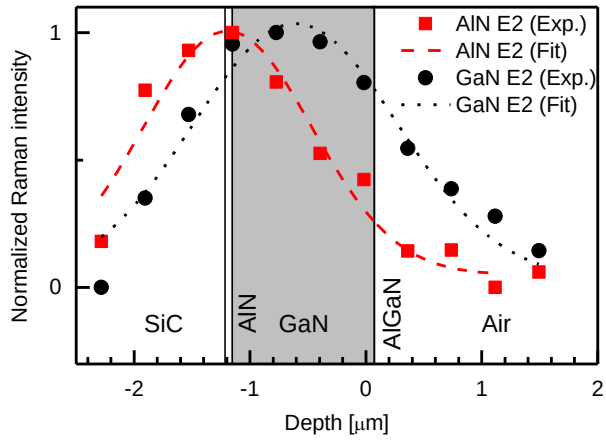

Figure 6: (a) Raman spectra measured by focusing at the center of a 1.2 μm-thick GaN layer from the top side (no SIL) and back side using a SIL. The Raman intensity is normalized to the SiC TO phonon peak to enable visual comparison of relative GaN epilayer and SiC substrate Raman intensity. Phonons originating from different layers in the device structure (labeled in (b)) are indicated. A magnified portion of the Raman spectra containing the AlN E_2 phonon peak is shown as an inset. (b) A SIL enhanced normalized Raman scattering intensity depth map showing the AlN E_2 and GaN E_2 peaks, measured through the highlighted AlGaN/GaN HEMT structure. Gaussian least squares fitted curves are overlaid as a visual aid.

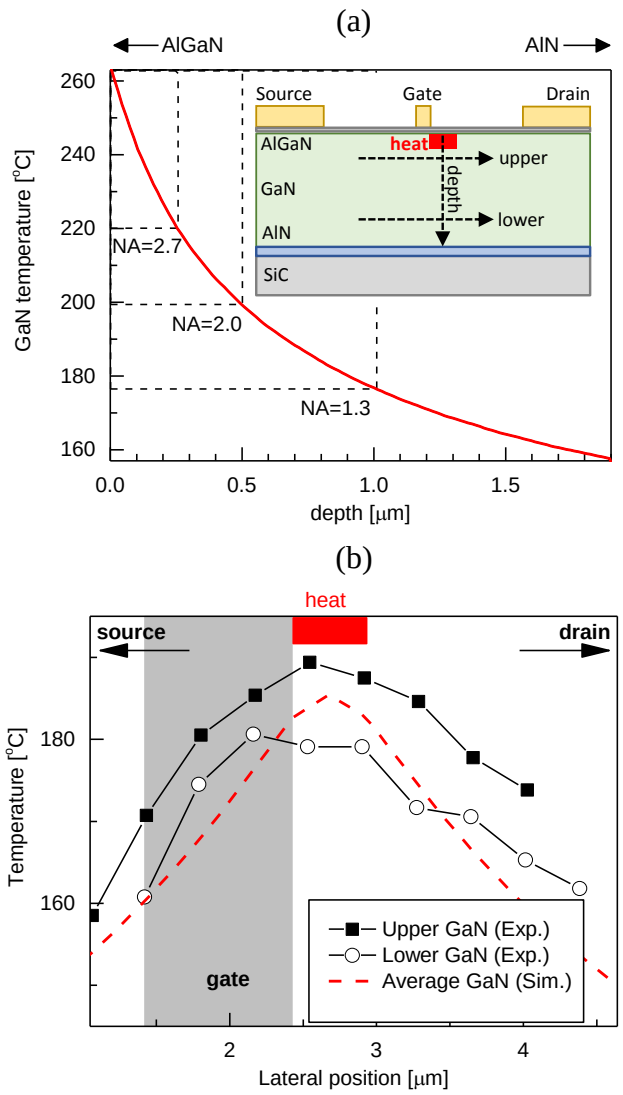

Figure 7: (a) Thermal simulation of the depth temperature profile (illustrated schematically as inset) through the GaN layer at the hottest location at the gate edge. The diffraction limited axial resolution for SiC h-SIL with an N.A. = 1.3, 2.0 and 2.7 (limit for SiC) are overlaid. Lateral temperature profile in the GaN layer in the vicinity of the gate measured by Raman thermography, measured through the SIL focusing onto the upper and lower portion of the GaN layer (illustrated schematically as an inset of (a)). The simulated depth averaged GaN temperature is also shown in (b). The 200μm-wide device was operated at a power dissipation density of 11.3 W/mm resulting in a total power dissipation of 2.26W.

REFERENCES

1 Y. F. Wu, A. Saxler, M. Moore, R. P. Smith, S. Sheppard, P. M. Chavarkar, T. Wisleder, U. K. Mishra, and P. Parikh, "30-W/mm GaNHEMTs by field plate optimization," Ieee Electr Device L **25** (3), 117-119 (2004).

2 J. W. Chung, W. E. Hoke, E. M. Chumbes, and T. Palacios, "AlGaN/GaN HEMT With 300-GHz f(max)," Ieee Electr Device L **31** (3), 195-197 (2010).

3 S. Rajasingam, J. W. Pomeroy, M. Kuball, M. J. Uren, T. Martin, D. C. Herbert, K. P. Hilton, and R. S. Balmer, "Micro-Raman temperature measurements for electric field assessment in active AlGaN-GaNHFETs," Ieee Electr Device L **25** (7), 456-458 (2004).

4 M. Kuball, J. M. Hayes, M. J. Uren, T. Martin, J. C. H. Birbeck, R. S. Balmer, and B. T. Hughes, "Measurement of temperature in active high-power AlGaN/GaN HFETs using Raman spectroscopy," Ieee Electr Device L **23** (1), 7-9 (2002).

5 A. Sarua, H. F. Ji, M. Kuball, M. J. Uren, T. Martin, K. J. Nash, K. P. Hilton, and R. S. Balmer, "Piezoelectric strain in AlGaN/GaN heterostructure field-effect transistors under bias," Appl Phys Lett **88** (10) (2006).

6 T. Batten, J. W. Pomeroy, M. J. Uren, T. Martin, and M. Kuball, "Simultaneous measurement of temperature and thermal stress in AlGaN/GaN high electron mobility transistors using Raman scattering spectroscopy," J Appl Phys **106** (9) (2009).

7 N. Shigekawa, K. Shiojima, and T. Suemitsu, "Optical study of high-biased AlGaN/GaN high-electron-mobility transistors," J Appl Phys **92** (1), 531-535 (2002).

8 E. Zanoni, F. Danesin, M. Meneghini, A. Cetronio, C. Lanzieri, M. Peroni, and G. Meneghesso, "Localized Damage in AlGaN/GaN HEMTs Induced by Reverse-Bias Testing," Ieee Electr Device L **30** (5), 427-429 (2009).

9 Richard Lossy, Arkadiusz Glowacki, Christian Boit, and Joachim Würfl, "Electroluminescence characterization of AlGaN/GaN HEMTs," physica status solidi (c) **6** (6), 1382-1385 (2009).

10 G. J. Riedel, J. W. Pomeroy, K. P. Hilton, J. O. Maclean, D. J. Wallis, M. J. Uren, T. Martin, and M. Kuball, "Nanosecond timescale thermal dynamics of AlGaN/GaN electronic devices," Ieee Electr Device L **29** (5), 416-418 (2008).

11 A. Sarua, H. Ji, K. P. Hilton, D. J. Wallis, M. J. Uren, T. Martin, and M. Kuball, "Thermal boundary resistance between GaN and substrate in AlGaN/GaN electronic devices," Ieee T Electron Dev **54** (12), 3152-3158 (2007).

12 Chris Hodges, J Anaya Calvo, Steve Stoffels, Denis Marcon, and M Kuball, "AlGaN/GaN field effect transistors for power electronics—Effect of finite GaN layer thickness on thermal characteristics," Appl Phys Lett **103** (20), 202108 (2013).

13 Nazli Donmezer and Samual Graham, "The impact of noncontinuum thermal transport on the temperature of AlGaN/GaN HFETs," Electron Devices, IEEE Transactions on **61** (6), 2041-2048 (2014).

14 M. Kuball, S. Rajasingam, A. Sarua, M. J. Uren, T. Martin, B. T. Hughes, K. P. Hilton, and R. S. Balmer, "Measurement of temperature distribution in multifinger AlGaN/GaN heterostructure field-effect transistors using micro-Raman spectroscopy," Appl Phys Lett **82** (1), 124-126 (2003).

15 A. Sarua, H. F. Ji, M. Kuball, M. J. Uren, T. Martin, K. P. Hilton, and R. S. Balmer, "Integrated micro-Raman/Infrared thermography probe for monitoring of self-heating in AlGaN/GaN transistor structures," Ieee T Electron Dev **53** (10), 2438-2447 (2006).

16 A. Manoi, J. W. Pomeroy, N. Killat, and M. Kuball, "Benchmarking of Thermal Boundary Resistance in AlGaN/GaN HEMTs on SiC Substrates: Implications of the Nucleation Layer Microstructure," Ieee Electr Device L **31** (12), 1395-1397 (2010).
17 M. Montes Bajo, C. Hodges, M. J. Uren, and M. Kuball, "On the link between electroluminescence, gate current leakage, and surface defects in AlGaN/GaN high electron mobility transistors upon off-state stress," Appl Phys Lett **101** (3) (2012).
18 N. J. Everall, "Modeling and measuring the effect of refraction on the depth resolution of confocal Raman microscopy," Appl Spectrosc **54** (6), 773-782 (2000).
19 S. M. Mansfield and G. S. Kino, "Solid Immersion Microscope," Appl Phys Lett **57** (24), 2615-2616 (1990).
20 M. Born and W. Wolf, *Principles of Optics*. (Pergamon, Oxford, 1970).
21 M. Baba, T. Sasaki, M. Yoshita, and H. Akiyama, "Aberrations and allowances for errors in a hemisphere solid immersion lens for submicron-resolution photoluminescence microscopy," J Appl Phys **85** (9), 6923-6925 (1999).
22 E. Ramsay, K. A. Serrels, M. J. Thomson, A. J. Waddle, R. J. Warburton, M. R. Taghizadeh, and D. T. Reid, "Three-dimensional nanometric sub-surface imaging of a silicon flip-chip using the two-photon optical beam induced current method," Microelectron Reliab **47** (9-11), 1534-1538 (2007).
23 T. Koyama, E. Yoshida, J. Komori, Y. Mashiko, T. Nakasuji, and H. Katoh, "High resolution backside fault isolation technique using directly forming Si substrate into solid immersion lens", in *IEEE Reliability Physics Symposium Proceedings 41, 2003.* (2003), pp. 529-535.
24 P. Scholz, N. Herfurth, M. Sadowski, T. Lundquist, U. Kerst, and C. Boit, "Efficient and flexible Focused Ion Beam micromachining of Solid Immersion Lenses in various bulk semiconductor materials – An adaptive calibration algorithm," Microelectron Reliab **54** (9–10), 1794-1797 (2014).
25 P Scholz, U Kerst, C Boit, CC Tsao, and T Lundquist, "Creation of solid immersion lenses in bulk silicon using focused ion beam backside editing techniques", in *Proceedings of the Symp. Testing and Failure Analysis., ASM International* (2008), pp. 157-162.
26 P Scholz, Uwe Kerst, Christian Boit, Chun-Cheng Tsao, and Ted Lundquist, "A Versatile design of solid immersion lenses in bulk silicon using focused ion beam techniques," Proc 35th ISTFA, 119-125 (2009).
27 P Scholz, C Gallrapp, Uwe Kerst, Ted Lundquist, and Christian Boit, "Optimizing focused ion beam created solid immersion lenses in bulk silicon using design of experiments," Microelectron Reliab **50** (9), 1441-1445 (2010).
28 S. Wilhelm, B. Gröbler, M. Gluch, and H. Heinz, *Confocal Laser Scanning Microscopy Principles*. (Carl Zeiss, Jena, 2000).
29 G. Adams, Winlens3D Basic (Qioptiq, 2015).
30 Virendra N. Mahajan, "Strehl ratio for primary aberrations in terms of their aberration variance," J. Opt. Soc. Am. **73** (6), 860-861 (1983).
31 C. A. Volkert and A. M. Minor, "Focused Ion Beam Microscopy and Micromachining," MRS Bulletin **32** (05), 389-399 (2007).
32 I. Chyr and A. J. Steckl, "GaN focused ion beam micromachining with gas-assisted etching," J Vac Sci Technol B **19** (6), 2547-2550 (2001).
33 C. Hodges, J. Pomeroy, and M. Kuball, "Probing temperature gradients within the GaN buffer layer of AlGaN/GaN high electron mobility transistors with Raman thermography," J Appl Phys **115** (6) (2014).

34 M. Stutzmann, O. Ambacher, A. Cros, M. S. Brandt, H. Angerer, R. Dimitrov, N. Reinacher, T. Metzger, R. Hopler, D. Brunner, F. Freudenberg, R. Handschuh, and C. Deger, "Properties and applications of MBE grown AlGaN," Mat Sci Eng B-Solid **50** (1-3), 212-218 (1997).

35 BB Goldberg, A Yurt, Y Lu, E Ramsay, FH Köklü, J Mertz, TG Bifano, and MS Ünlü, "Chromatic and spherical aberration correction for silicon aplanatic solid immersion lens for fault isolation and photon emission microscopy of integrated circuits," Microelectron Reliab **51** (9), 1637-1639 (2011).